DOI: 10.1002/chem.200800050

VIP

Phosphorescent Iridium(III) Complexes with Nonconjugated Cyclometalated Ligands

Yi-Hwa Song,[a] Yuan-Chieh Chiu,[a] Yun Chi,*[a] Yi-Ming Cheng,[b] Cheng-Hsuan Lai,[b] Pi-Tai Chou,*[b] Ken-Tsung Wong,[b] Ming-Han Tsai,[c] and Chung-Chih Wu*[c]

Abstract: A series of blue phosphorescent iridium(III) complexes **1–4** with nonconjugated N-benzylpyrazole ligands were synthesized and their structural, electrochemical, and photophysical properties were investigated. Complexes **1–4** exhibit phosphorescence with yields of 5–45% in degassed CH_2Cl_2. Of the compounds, **1** showed emission that was nearly true blue at 460 nm with a lack of vibronic progression. These photophysical data clearly demonstrate that the methylene spacer of the cyclometalated N-benzylpyrazole chelate effectively interrupts the π conjugation upon reacting with a third L^X chelating chromophore. This gives a feasible synthesis for the blue phosphorescent complexes with a sufficiently large energy gap. In another approach, these complexes were investigated for their suitability for the host material in phosphorescent OLEDs. The device was synthesized by using **1** as the host for the green-emitting [Ir(ppy)$_3$] dopant, which exhibits an external quantum conversion efficiency (EQE) of up to 11.4% photons per electron (and 36.6 cdA^{-1}), with 1931 Commission Internationale de L'Eclairage (CIE) coordinates of (0.30, 0.59), a peak power efficiency of 21.7 lmW^{-1}, and a maximum brightness of 32000 cdm^{-2} at 14.5 V. At the practical brightness of 100 cdm^{-2}, the efficiency remains above 11% and 18 lmW^{-1}, demonstrating its great potential as the host material for phosphorescent organic light-emitting diodes.

Keywords: conjugation · cyclometalation · energy transitions · iridium · phosphorescence

Introduction

Phosphorescent organic light-emitting diodes (OLEDs) are under intensive investigation due to their potential for improving device brightness and performance.[1] In contrast, with the fluorescent emission, the electrophosphorescence is easily harnessed from both singlet and triplet excited states and, thus, their internal quantum efficiency can reach a theoretical level of unity, rather than the 25% inherent upper limit imposed by the formation of singlet excitons for the respective fluorescent materials.[2] Thus, a great deal of effort has been made on the second- and third-row transition metal complexes for developing highly efficient phosphors that can emit all three primary colors.

Despite the expanse of research on both red and green phosphors, there are relatively few reports on the room-temperature blue phosphorescence.[3] The seminal example should be credited to the iridium(III) complex named as **FIrpic**, which has proved to be an excellent dopant for sky-blue phosphorescent OLEDs.[4,5] Further improvements were made by substituting picolinate with other ancillary ligands, such as tetrakis(1-pyrazolyl) borate. to afford **FIr6**[6] and even pyridyl azolate ligands to afford **FIrtaz** and various derivatives.[7] These modifications have produced a further hypsochromic shift of approximately 10 nm versus the emission of **FIrpic**; however, their significant lowering of the quantum yield (QY) has hampered the fabrication of the highly efficient, true-blue phosphorescent OLEDs. To ach-

[a] Dr. Y.-H. Song, Y.-C. Chiu, Prof. Y. Chi
Department of Chemistry, National Tsing Hua University
Hsinchu 300 (Taiwan)
Fax: (+886) 3-572-0864
E-mail: ychi@mx.nthu.edu.tw

[b] Dr. Y.-M. Cheng, C.-H. Lai, Prof. P.-T. Chou, Prof. K.-T. Wong
Department of Chemistry, National Taiwan University
Taipei 106 (Taiwan)
Fax: (+886) 2-2369-5208
E-mail: chop@ntu.edu.tw

[c] M.-H. Tsai, Prof. C.-C. Wu
Department of Electrical Engineering
Graduate Institute of Photonics and Optoelectronics
and Graduate Institute of Electronics Engineering
National Taiwan University, Taipei 106 (Taiwan)
Fax: (+886) 2-2367-7467
E-mail: chungwu@cc.ee.ntu.edu.tw

Supporting information for this article is available on the WWW under http://www.chemeurj.org/ or from the author.

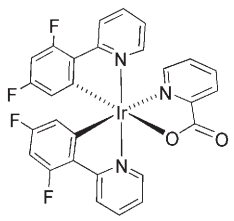

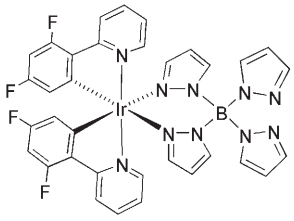

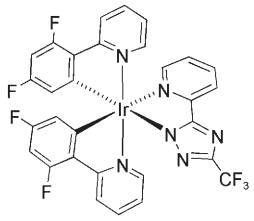

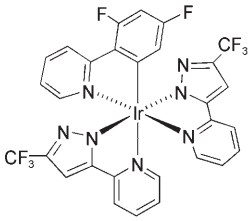

ieve this goal, further modification of the molecular design has to be considered. Recently, isomeric iridium complexes [Ir(dfppy)(fppz)$_2$][8] (dfppyH = 2-(4,6-difluorophenyl)pyridine; fppzH = 3-trifluoromethyl-5-(2-pyridyl)pyrazole) have been reported that show a coordination environment based on one dfppy and two fppz ligands. Notably, this complex produced a hypsochromic shift of approximately 20 nm compared with the phosphorescence of **FIrpic** in solution, thus serving as the best candidate so far for the fabrication of blue OLED devices.

Note, almost all of abovementioned iridium blue phosphors possess at least one dfppy ligand as their intrinsic luminescence chromophore. The relatively fixed energy gap would encounter a severe limitation for its further extension to saturated blue. One main obstacle lies in the direct crosstalk, that is, conjugation, between, for example, difluorobenzyl (HOMO) and pyridyl (LUMO) moieties in dfppy. As such, the conjugation leads to the increase (decrease) of HOMO (LUMO) orbital energy. Moreover, due to the conjugation, tuning the energy gap by substitution on one side (e.g. HOMO) commonly renders adverse effect on the other side (e.g. LUMO). This results in a slight or even negligible gain in the desired energy gap. To overcome this intrinsic restriction, one strategy is to design a nonconjugated bidentate ligand, in which two designated moieties are strategically linked by a saturated σ-bond spacer to minimize the crosstalk. Herein, we report a new design for the Ir^{III} dimeric intermediates [Ir(μ-Cl)(dfb-pz)$_2$]$_2$ and [Ir(μ-Cl)(tfmfb-pz)$_2$]$_2$, which employ two nonconjugated cyclometalated ligands, namely, 2,4-difluorobenzyl-*N*-pyrazole ((dfb-pz)H) and 2-trifluoromethyl-5-fluorobenzyl-*N*-pyrazole ((tfmfb-pz)H). The ligands are assembled by linking two aromatic chromophores with a saturated methylene spacer (Scheme 1). We propose that the methylene unit in both dfb-pz and tfmfb-pz ligands would effectively interrupt the π conjugation, the results of which are expected to be a lowering in the relative energy of ligand-centered π orbitals and the destabilization of the respective π* orbitals. Thus, upon reacting with a third, L^X chelating chromophore with a sufficiently larger energy gap, we can systematically synthesize a new series of organometallic complexes that show the required saturated-blue phosphorescent emission. Herein, we report the preparation, basic photophysical properties, and the unexpected isomerization in solution that is caused by the restricted twisting motion involving the methylene units. The applications of these Ir^{III} complexes, which are prepared by using such design strategies are also elaborated.

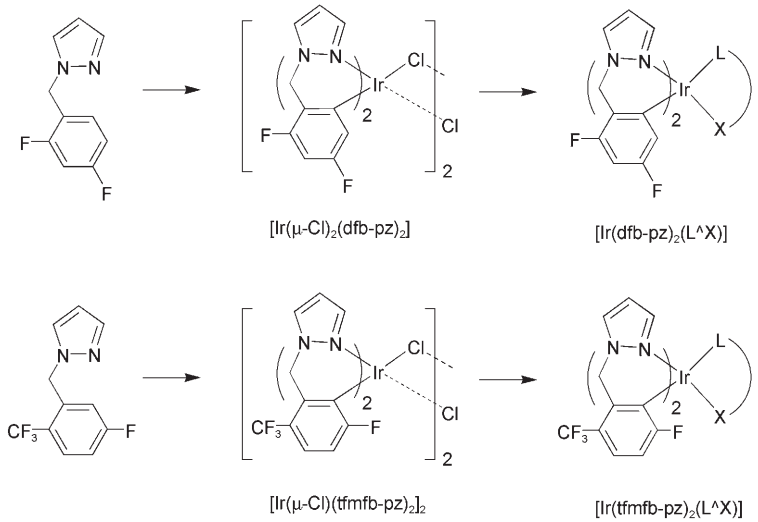

Scheme 1. Assembly of the ligands for the Ir^{III} dimeric intermediates [Ir(μ-Cl)(dfb-pz)$_2$]$_2$ and [Ir(μ-Cl)(tfmfb-pz)$_2$]$_2$.

Results and Discussion

Synthesis and characterization: Preparation of emissive complexes **1–3** was executed in a one-pot concept by heating of a 2:1 mixture of nonconjugated ligand (dfb-pz)H and [IrCl$_3$]·3H$_2$O in methoxyethanol (140 °C, 24 h) followed by the addition of 1 equivalent of chelate (L^X)H in presence of proton scavenger Na$_2$CO$_3$ (RT, 12 h). The products are separated by silica-gel column chromatography, eluting with a 1:1 mixture of CH$_2$Cl$_2$ and hexane. It is believed that the reaction proceeded through a dimeric intermediate with formula [Ir(μ-Cl)(dfb-pz)$_2$]$_2$. Afterwards, addition of the chelat-

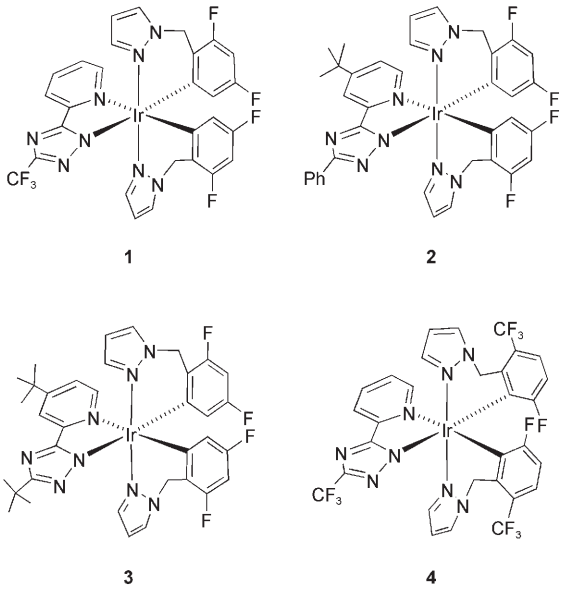

1 2 3 4

ing anion (L^X) would induce the in situ cleavage of the dimer[9] to give the monometallic products with formula [Ir(L^X)(dfb-pz)$_2$]. Similarly, compound **4** was prepared by employing the distinctive nonconjugated cyclometalated ligand (tfmfb-pz)H. Note, that if the second reaction with the L^X ligand was conducted in refluxing methoxyethanol rather than stirring at room temperature, a notable reduction in product yields was observed, the result of which showed the intricate nature of such synthetic approaches.

All these complexes were characterized by using ^{1}H NMR and ^{19}F NMR spectroscopy. Interestingly, their room temperature ^{1}H NMR spectra in the region of the methylene group showed broadened peaks in the region of $\delta = 5.80$–5.12 ppm, which indicates the occurrence of rapid fluxional motion. This phenomenon was further confirmed by variable-temperature ^{19}F NMR spectroscopy experiments. For example, the ^{19}F NMR spectrum of **1** exhibited two sets of CF_3 signals at $\delta = -63.51$ and -63.34 ppm with a ratio of 15:1 at $-60\,^\circ$C, which indicates the existence of two isomers. The respective C–F signals occurred at $\delta = -115.01$, -115.56, -117.53, and -119.53 ppm and another set of less-intense signals at $\delta = -113.15$, -115.13, -117.71, and -119.16 ppm (Figure 1), which were confirmed by showing an identical integration ratio with that of the CF_3 signals. However, upon an increase of the temperature to 0 °C, all signals of the minor isomer merged into the baseline, whereas the two downfield signals at $\delta = -115.16$ and -115.90 ppm of the major isomer turned significantly broader relative to other signals. The relative dfb-pz derivatives **2** and **3** exhibit similar temperature-dependent behavior, which confirms the existence of a second isomer. Unfortunately, no details regarding their structural properties can be deciphered by using these spectral data.

Similar to that of **1**–**3**, complex **4** also showed the existence of two isomers in solution. This is exemplified by the ^{19}F NMR spectrum that was recorded in $CDCl_3$ solution in

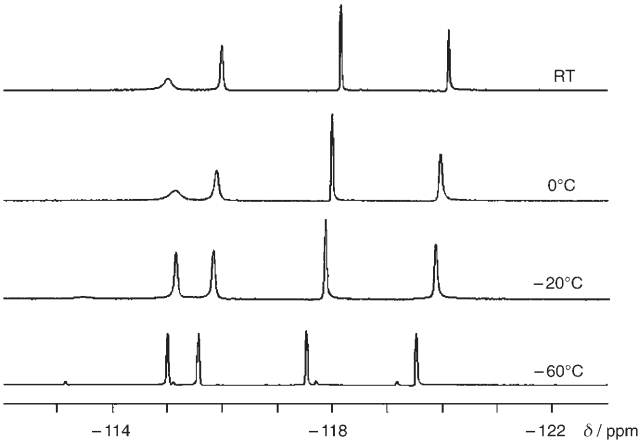

Figure 1. Variable-temperature ^{19}F NMR spectra of complex **1** recorded in [D$_6$]acetone. These spectra show the region of aryl C–F resonances.

which two pairs of nearly equal intensity aryl C–F signals were observed in $CDCl_3$ solution at room temperature and which showed a 1:1 ratio of the two isomers (Figure 2). This

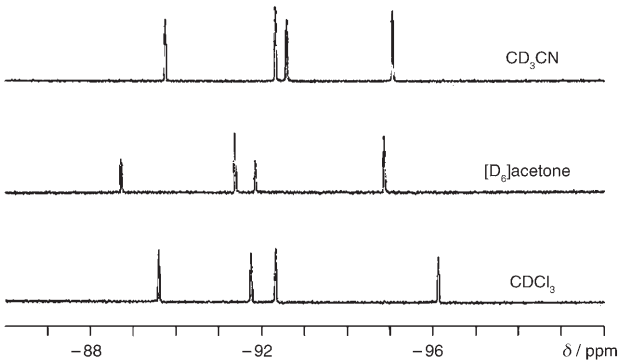

Figure 2. ^{19}F NMR spectra of **4** recorded in $CDCl_3$, [D$_6$]acetone, and CD_3CN solution. These spectra show a 1:1, 1:1.7, and 1:1.3 ratio of isomers, respectively. Note that only the resonances for the aryl C–F groups are depicted for simplicity.

isomerization was also assured by changing the solvent to [D$_6$]acetone and CD_3CN, from which distinctive integration ratios of 1:1.7 and 1:1.3 were detected, showing its drastic dependence on the nature of the solvent. Again, explicit structural features of these isomers remained unknown.

A single X-ray crystal structure diffraction study was then carried out to reveal the exact structures of **1** and **4**, as well as the possible cause for the solution isomerism. As displayed in Figure 3, compound **1** showed slightly distorted octahedral geometry with two cyclometalated dfb-pz ligands and one pyridyl triazolate (fptz) chelate surrounding the iridium metal center. It is notable that the N-pyrazolyl group of the dfb-pz ligand is located in the mutual *trans* orientation, whereas the dfb substituents reside in the *cis* disposition, thereby showing the typical configuration that was observed in many heteroleptic complexes.[2b,10] Moreover, the methylene spacer of both dfb-pz ligands is bent away from

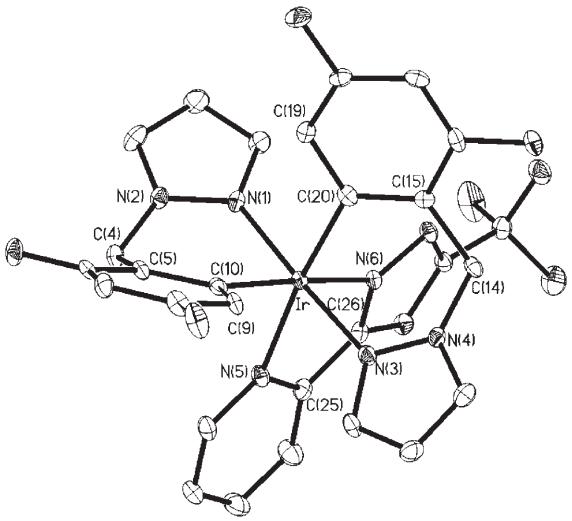

Figure 3. ORTEP diagram of **1** with thermal ellipsoids shown at the 50% probability level; selected bond distances: Ir–N(1) = 2.039(4), Ir–N(3) = 2.028(4), IrN(5) = 2.181(4), Ir–N(6) = 2.116(4), Ir–C(10) = 2.039(4), Ir–C(20) = 2.024(4) Å.

the dfb groups of the other cyclometalated ligand. This could be due to the excessive non-bonding interaction between the atoms; compare C(4)···H(19)–C(19) = 3.681 Å and C(14)···H(9)–C(9) = 3.932 Å. On the other hand, the fptz chelate is located opposite to both of the cyclometalated dfb segments. The associated Ir–N distances (Ir–N(5) = 2.181(4) and Ir–N(6) = 2.116(4) Å) are significantly longer than the mutually *trans*-disposed Ir–N distances (Ir–N(1) = 2.039 and Ir–N(3) = 2.028 Å). This observation confirmed the *trans* effect that is imposed by the dfb segments within this class of Ir^{III}-cyclometalated complexes.[11]

An X-ray crystal structural characterization of **4** was then conducted to determine the difference in structure compared with **1**. As shown in Figure 4, although the coordination geometry around the Ir^{III} metal atom is essentially identical to that **1**, the Ir–C distances, Ir–C(21) = 2.045(4) and Ir–C(10) = 2.064(4) Å, are slightly longer than those of the Ir–C bond observed in **1**, Ir-C(20) = 2.024(4) and Ir-C(10) = 2.039(4) Å. This is obviously attributed to the intrinsic nature of the benzyl functional group, tfmfb. In addition, the methylene spacers of both tfmfb-pz chelates are pointing toward the benzyl group of adjacent tfmfb-pz chelates. This conformation is in sharp contrast with complex **1**, for which the respective methylene spacers are leaning away from the benzyl group of their adjacent nonconjugated chelate, and pointing to the opposite direction from where the third ancillary ligand is located.

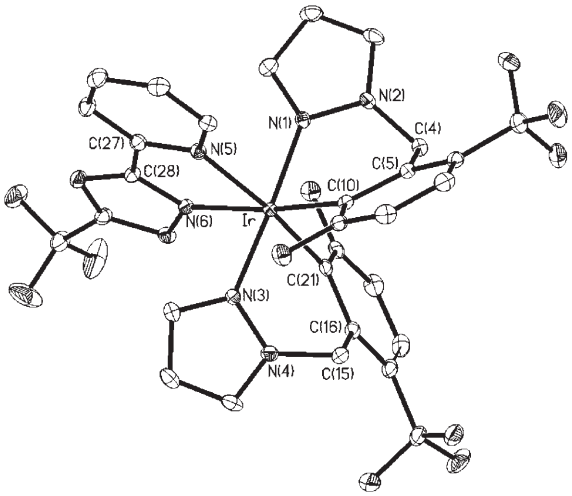

Figure 4. ORTEP diagram of **4** with thermal ellipsoids shown at the 50% probability level; selected bond distances: Ir–N(1) = 2.042(3), Ir–N(5) = 2.174(3), Ir–N(6) = 2.089(3), Ir–N(3) = 2.027(3), Ir–C(21) = 2.045(4), Ir–C(10) = 2.064(4) Å.

The two orientations of the methylene groups in **1** and **4** offer a simple and rational explanation for the conformational isomerism that was detected in the solution phase, for which the ligand dynamics are akin to those observed for the inversion of 6-membered palladocycles in the cyclopalladated derivatives of 2-benzylpyridine.[29] Moreover, according to the X-ray crystal structure analyses, it is presumed that the two isomers that are observed in ^{19}F NMR spectroscopy probably exhibited similar structural features observed for compounds **1** and **4**. At room temperature, it seems that the rate of dynamic equilibrium between isomers for **1** is much faster than that for **4**. Such a difference might be rationalized by the existence of the *ortho*-fluorine substituent on the benzyl moieties. As shown in Figure 5, a closer non-

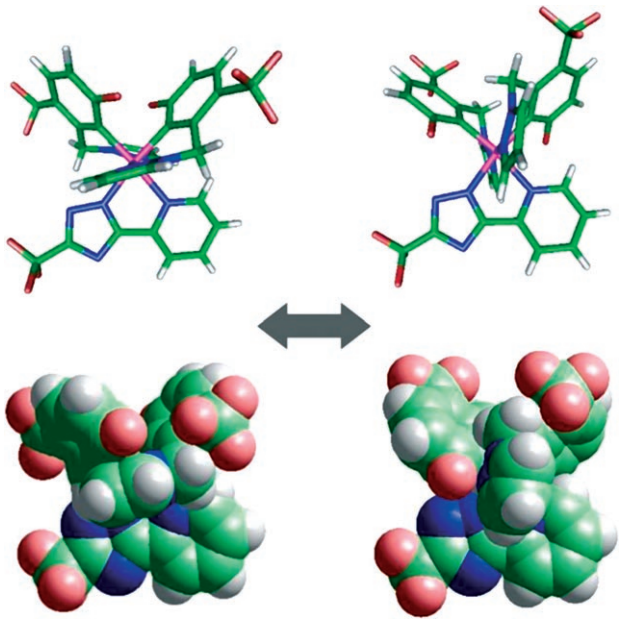

Figure 5. Computer-generated structural diagrams that show the two isomers of **4** in CH_2Cl_2 solution.

bonding contact between the unique fluorine atom of the tfmfb-pz chelate and other adjacent chelates was anticipated upon inspecting the computer-generated, ball-and-stick and space-filling diagrams of two conformational isomers of **4**. These unique *ortho*-substituted fluorine atoms would experi-

ence an even greater steric barrier while isomerization occurred, that is, rotation of the nearby Ir–$C_{(benzyl)}$ vectors is required and results in an increase in activation energy and, as a consequence, two pairs of slowly interchangeable ^{19}F NMR spectroscopy signals at room temperature are produced.

Photophysical properties: The UV/Vis absorption and emission spectra of complexes **1**–**4** in CH_2Cl_2 at 298 K are shown in Figure 6. All the spectroscopic data are tabulated in

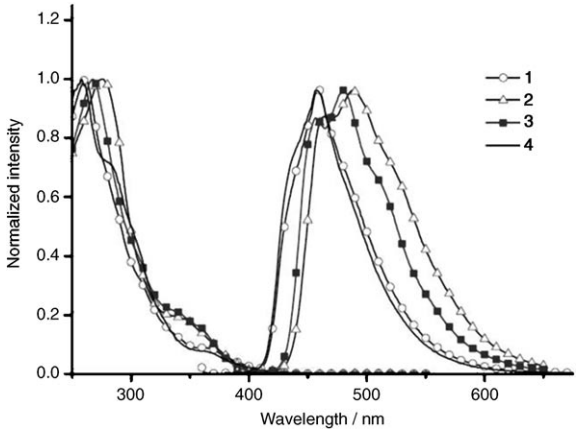

Figure 6. The normalized UV/Vis absorption and emission spectra of **1**–**4** in CH_2Cl_2 at room temperature.

Table 1. The investigated complexes all show a very similar pattern in the absorption spectra. The absorption bands ranging from 260–280 nm can be ascribed to π–π* intraligand charge-transfer (^{1}ILCT) transitions due to their intense molar extinction coefficient ε of greater than $10^4\,M^{-1}cm^{-1}$, whereas the weaker transitions ($\varepsilon \approx 10^3\,M^{-1}cm^{-1}$) at longer wavelengths (in the range of 350–365 nm) are attributed to the spin-allowed metal-to-ligand charge transfer (^{1}MLCT) mixed with a certain extent of ligand-centered (LC) charge-transfer transitions (see below).

Spectacularly, **1** reveals a blue emission with a peak wavelength at 460 nm. A remarkable feature of this emission lies in its lack of a spectral shoulder in the region of approximately 490 nm, making **1** a truly deep-blue emitter (see below). Note that the vibronic shoulder at approximately 490 nm appeared in the well-known blue emitting Ir^{III} complex **FIrtaz** and its related derivatives;[12] this results in the inferiority to achieve a true-blue hue. As for the rest of the investigated complexes **2**–**4**, they all also display an intense phosphorescence band maximized at the range of 450–490 nm with quantum yields of 5–45 % and radiative decay-rate constants of greater than $10^5\,s^{-1}$ (see Table 1). For **2**, the phenyl functional group on the triazolate moiety results in an approximately 8 nm bathochromic-shifted emission with respect to **3**. The result can be rationalized by the additionally extended phenyl π-conjugation system in **2**, which increases the π orbital energy of the triazolate moiety.[12] As discussed in the following section of the theoretical approach, the HOMO (π component) of **2** is mainly located at the phenyl-triazolate, which is quite different from **1** and **4** in which the HOMO is located at the substituted benzyl moiety. In the case of **3**, the substitution effects resulting from the electron-donating *tert*-butyl substituents destabilize the HOMO to a larger extent than that of the LUMO, and, hence, lead to a much-reduced transition gap as compared with complexes **1** and **4**. Evidence for this is further supported by a non-negligible contribution of the triazolate to the HOMO versus none for **1** and **4**. We also noticed that different substitutions on the benzyl group of the nonconjugated ligands rendered minor influences on the spectral features. For example, the CF_3 functional group in complex **4**, which was supposed to be a better electron acceptor than a fluorine atom, only caused the emission peak wavelength to be blue shifted from approximately 460 nm of complex **1** to approximately 457 nm.

To gain insight into the photophysical behavior of all of the titled complexes, DFT was applied to molecular orbital studies. As a result, those HOMO and LUMO orbitals that are mainly involved in the lowest-lying transitions are depicted in Figure 7, whereas more-selected molecular orbitals are shown in Figure S1 in the Supporting Information. A description of the energy gap of each transition and the frontier orbital compositions for the involved orbitals are listed in Tables 2 and 3, respectively. These results, especially the calculated energy gaps, agree satisfactorily with the experimental photophysical data, suggesting that the time-dependent DFT (TD-DFT) calculations can, to a certain degree,

Table 1. Photophysical and electrochemical data for complexes **1**–**4**.

		Photophysical Properties[a]					Electrochemical data [V][b]	
Complex	$A\ \lambda_{max}$ [nm] ($\varepsilon \times 10^{-3}$)	$E_m\ \lambda_{max}$ [nm]	Φ [%]	τ_{obs} [μs]	$k_r \times 10^6$	$k_{nr} \times 10^6$	E_{pa}^{ox}	E_{pc}^{red}
1	261 (23.0), 368 (1.8)	437, 460	10	0.10	1.0	9	1.00	−2.55
2	276 (43.8), 343 (8.5)	464, 488	45	2.77	0.2	0.2	0.85	−2.74
3	267 (28.1), 340 (5.6)	456, 480	20	1.23	0.2	0.7	0.83	−3.11
4	261 (21.8), 284 (15.4), 370 (1.4)	434, 457	4	0.07	0.6	14	1.09	−2.53

[a] Data were recorded in a degassed CH_2Cl_2 solution at room temperature with ε in $M^{-1}\,cm^{-1}$. [b] All electrochemical potentials were measured in a CH_2Cl_2 and THF solution with 0.1 M tetrabutylammonium hexafluorophosphate ($TBAPF_6$) for the oxidation and reduction measurement, and reported in volts by using Fc/Fc^+ (Fc/Fc^+ = ferrocene/ium) as the reference. The Pt electrode and Au(Hg) alloy were selected as the working electrode for the oxidation and reduction processes, respectively. E_{pa}^{ox} represents the irreversible anodic peak potential, whereas E_{pc}^{red} represents the irreversible cathodic peak potential. E_m is the emission, $k_r = \Phi/\tau_{obs}$, and $k_{nr} = (1/\tau_{obs}) - k_r$.

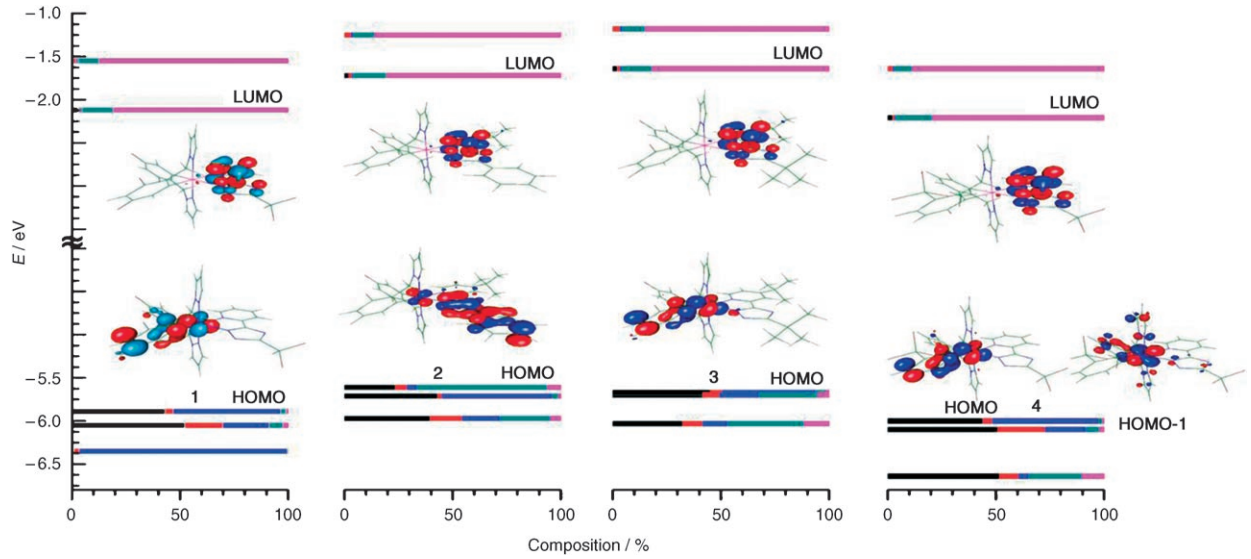

Figure 7. Schematic representation of the calculated electron structure and the frontier orbitals in the gas phase for complexes **1**–**4** at their S_0-optimized geometries. Colors of the bar compositions: black (Ir), red (pyrazole in dfb-pz or tfmfb-pz), blue (benzyl in dfb-pz or tfmfb-pz), green (triazolate in fptz, pbptz, or bbptz), magenta (pyridyl in fptz, pbptz, or bbptz). Also shown are the isodensity surface contours of the HOMO and LUMO of complexes **1**–**4**.

Table 2. Transitions of **1**–**4** calculated with the TD-DFT method in CH_2Cl_2 solution upon employing the polarized continuum model.

Entry	States	λ	f	Configuration	Assignment[a]
1	T_1	404.9	0	HOMO−2→LUMO (+61%) HOMO−1→LUMO (16%) HOMO−6→LUMO (12%) HOMO−3→LUMO (6%) HOMO−6→LUMO+1(5%)	MLCT/LLCT
	S_1	370.2	0.0051	HOMO→LUMO (+88%) HOMO−1→LUMO (+10%)	MLCT/LLCT
2	T_1	442.9	0	HOMO→LUMO (+80%) HOMO−2→LUMO (+9%) HOMO→LUMO+1 (+7%)	MLCT/ILCT
	S_1	370.9	0.1041	HOMO→LUMO (+90%)	MLCT/ILCT
3	T_1	428.7	0	HOMO→LUMO (+54%) HOMO−2→LUMO (33%) HOMO→LUMO+1 (+9%)	MLCT/LLCT/ILCT
	S_1	359.5	0.085	HOMO→LUMO (+93%)	MLCT/LLCT
4	T_1	405.7	0	HOMO−2→LUMO (+64%) HOMO−1→LUMO (14%) HOMO−5→LUMO (8%) HOMO→LUMO (8%)	MLCT/ILCT
	S_1	371.0	0.002	HOMO−1→LUMO (+80%) HOMO→LUMO (18%)	MLCT/LLCT

[a] The assignment is based on the predominant transitions.

predict the photophysical behavior of these iridium complexes. As depicted in Figure 7, the patterns of the occupied orbitals are essentially the same in complexes **1**, **3**, and **4**, with the HOMO orbital being a combination of iridium and benzyl (in dfb-pz or tfmfb-pz ligand) orbitals. Nevertheless, we note a rather small but non-negligible contribution from the triazolate, which indicates that the addition of the electron-donating *tert*-butyl group indeed increases the π orbital energy of the triazolate moiety. This becomes more obvious for **2**, in which the presence of a phenyl group anchored on the triazolate moiety elongates the π conjugation and hence its HOMO π energy is greatly increased. As a result, the HOMO orbital of **2** is not located at the benzyl (in dfb-pz ligand) orbitals but rather at the triazolate moiety (see Figure 7). For both cases of **2** and **3**, it is reasonable to expect that the calculated emission gap is smaller than that of **1** and **4**, which is consistent with the experimental results. On the other hand, the pattern of the lowest-lying virtual orbitals for complexes **1**–**4** is almost the same, being predominately composed of the pyridyl moiety in the fptz, pbptz, or bbptz ligands (see Figure 7). The results reflect that the lowest-lying electronic transition (S_1 and T_1) of **1**–**4** is mainly ascribed to MLCT (d_π→pyridyl fragment) mixed with a certain extent of π–π* ligand-centered charge-transfer (ILCT or LLCT). The results also implied that the substituent on the benzyl and/or pyridyl part of the ligands in all the investigated complexes played a key role in the alternation of energy levels of the occupied and/or virtual orbitals.

We also noticed that the orbital compositions of HOMO and LUMO for complexes **1** and **4** are essentially the same. Furthermore, both the HOMO and LUMO of **4** are more or less stabilized as compared with **1** because of the CF_3 group on the benzyl moiety, which acts as an electron acceptor. However, TD-DFT calculations gave results of similar energy gaps but with different transition configurations

Table 3. Molecular orbital compositions in the ground state for complexes **1**–**4** at the B3LYP level.

Orbital	Energy [eV]	MO composition [%] Ir	Pyrazole (C^N)	Benzyl (C^N)	Triazolate (L^X)	Pyridyl (L^X)	Characteristics
complex **1**							
LUMO+1	−1.55	0.29	1.55	1.03	9.73	87.41	π*(fptz)
LUMO	−2.12	2.77	1.02	0.78	14.63	80.79	π*(fptz)
HOMO–LUMO energy gap							
HOMO	−5.89	43.22	3.65	49.61	2.39	1.12	d(Ir)+π(dfb-pz)
HOMO−1	−6.05	52.17	17.57	21.52	6.3	2.44	d(Ir)+π(dfb-pz)
HOMO−2	−6.35	1.02	2.29	96.31	0.37	0.02	d(Ir)+π(dfb-pz)
complex **2**							
LUMO+1	−1.25	0.25	2.66	1.28	9.69	86.12	π*(pbptz)
LUMO	−1.72	2.15	1.05	0.94	15.23	80.64	π*(pbptz)
HOMO–LUMO energy gap							
HOMO	−5.61	23.5	5.25	4.63	60.47	6.15	d(Ir)+π(pbptz)
HOMO−1	−5.71	43.11	1.81	51.03	3.07	0.99	d(Ir)+π(dfb-pz)
HOMO−2	−5.97	39.49	14.71	17.55	23.49	4.76	d(Ir)+π(pbptz)
complex **3**							
LUMO+1	−1.18	0.23	2.93	1.25	10.5	85.1	π*(bbptz)
LUMO	−1.64	2.14	1.15	1	13.8	81.91	π*(bbptz)
HOMO–LUMO energy gap							
HOMO	−5.67	45.19	5.34	43.24	4.98	1.25	d(Ir)+π(dfb-pz)
HOMO−1	−5.7	41.58	7.82	18.2	27.16	5.24	d(Ir)+π(bbptz)
HOMO−2	−6.03	32.36	9.1	11.56	35.43	11.55	d(Ir)+π(bbptz)
complex **4**							
LUMO+1	−1.64	0.27	1.75	1.21	8.14	88.63	π*(fptz)
LUMO	−2.21	2.27	0.76	0.73	16.76	79.47	π*(fptz)
HOMO–LUMO energy gap							
HOMO	−6.00	43.87	4.32	49.42	1.56	0.82	d(Ir)+π(tfmfb-pz)
HOMO−1	−6.10	50.98	21.79	18.74	6.26	2.22	d(Ir)+π(tfmfb-pz)
HOMO−2	−6.64	51.79	8.66	4.77	24.48	10.29	d(Ir)+π(fptz)

(Table 2). For example, the $S_0 \rightarrow S_1$ transition of **1** is composed of an 88% HOMO to LUMO transition, whereas the dominant transition is from HOMO−1 to LUMO (80%) in **4**. In addition, the HOMO−1 of **4** is no longer predominated by only the benzyl moiety (except for the contribution from central metal atom) but with an equal amount of populations from both triazolate and benzyl fragments. We tentatively ascribed the differences in TD-DFT prediction to the imperfection of the solvation model (polarized continuum model, see the Experimental Section) adopted in this study and suspected that the configuration of these methylene-spacer-imposed Ir^{III} complexes might be greatly influenced by the solvation effect. However, applying an advanced solvent model, such as explicit solvation,[13] based on an ab initio approach is not realistic at this stage. For complex **2**, the triazolate-based HOMO is considerably destabilized with respect to the benzyl HOMO−1 as an effect of the more-elongated π conjugation on the triazolate moiety (see Table 3). Regarding complex **3**, as shown in Figure 7, the LUMO is destabilized relative to **1** because of the presence of an electron-donating *tert*-butyl substituent on the pyridyl group. This, in combination with a similar HOMO energy level between **1** and **3**, leads to a relatively large transition gap in **3** (compare with **1**).

The above results clearly demonstrate the concept of introducing a spacer into the cyclometalated ligand to break the π conjugation of chelating ligands. The net result then lowers the energy level of the π orbitals and destabilizes the respective π* orbitals of the ligands. Accordingly, the emission wavelength can be fine tuned through the substituent effect without taking much account of the interplay between the HOMO and LUMO due to the crosstalk and thereby simplifying the chemical modification and interpretation. With the assistance of this basic designing principle and the incorporation of the third chelating chromophores with an appropriate energy gap, desired emission color can thus be successfully prepared.[14]

Electrochemistry: The electrochemical behavior of these Ir metal complexes was investigated by cyclic voltammetry by using ferrocene as the internal standard, and the results are summarized in Table 1. During the anodic scan in CH_2Cl_2, all complexes exhibit an irreversible oxidation peak in the region of 0.83–1.09 V. It is believed that the oxidation occurred mainly at the iridium metal center, concomitant with contributions from the surrounding chelates. Accordingly, the strong electron-withdrawing CF_3 substituent on the triazolate fragment led to the decrease in their oxidation potentials. This is demonstrated by the higher oxidation potential of **1** (1.00 V) relative to that of **2** (0.85 V) and **3** (0.83 V), which possess phenyl and *t*-butyl substituents. Moreover, comparison of the oxidation peak potentials between **1** (1.00 V) and **4** (1.09 V) revealed that tfmfb-pz has more in electron-withdrawing strength than its dfb-pz counterpart.

Table 4. Performance data of OLED devices A, B, and C.

Devices	A1	A2	B1	B2	C
voltage [V][a]	14	8.2	9.6	9.2	9
brightness [cdm^{-2}][a]	314	307	230	592	5020
EQE [%][a]	1.4	0.8	0.8	1.3	7.1
LE [cdA^{-1}][a]	1.7	1.5	1.2	2.9	22.9
max brightness	2014 at 20 V	2387 at 13 V	1882 at 15 V	3835 at 14 V	31560 at 15 V
max EQE [%]	2.3	1.3	1.0	1.5	11.4
max LE [cdA^{-1}][b]	2.9	2.5	1.5	3.4	36.6
max PE [lmW^{-1}][b]	1.5	1.9	0.9	1.9	21.7
EL λ_{max} [nm][c]	460	460	461	460	509
CIE (x, y)[c]	0.19, 0.21	0.21, 0.30	0.18, 0.22	0.26, 0.37	0.30, 0.59

[a] Measured at a current density of 20 mAcm^{-2}. [b] LE is the luminance efficiency and PE is the power efficiency. [c] With the applied driving voltage at 9 V.

Upon switching to the cathodic sweep in THF, irreversible waves were also detected in all cases. In contrast with the oxidation process, the reduction may occur primarily on the low-lying π* orbitals of the pyridyl segment of the ancillary azolate chelate. Thus, the largest negative potential for **3** (−3.11 V) could be rationalized by the possession of two electron-donating *tert*-butyl substituents.

Device results: To evaluate the electroluminescent properties of the developed iridium complexes, several electroluminescent (EL) devices were fabricated by using complexes **1** and **3** as dopant emitters. The devices were fabricated on glass substrates with the typical structure of multiple organic layers sandwiched between the bottom indium tin oxide (ITO) anode and the top metal cathode (Al). The device structure used for device A1 was ITO/αNPD (200 Å)/TCTA (200 Å)/CzSi (200 Å)/10% **1** in UGH2 (200 Å)/TAZ (500 Å)/LiF (5 Å)/Al (1200 Å). For device A2, the device structure was ITO/αNPD (300 Å)/TCTA (50 Å)/CzSi (50 Å)/10% **3** in UGH2 (100 Å)/BCP (500 Å)/LiF (5 Å)/Al (1200 Å), for which 4,4′-bis[*N*-(1-naphthyl)-*N*-phenyl-amino]biphenyl (αNPD) and 4,4′,4″-tri(*N*-carbazolyl)triphenylamine (TCTA) were used as the hole-transport layers,[8] whereas a CzSi layer[8] was applied for improving hole transport and for blocking the high-energy triplet excitons (on **1** and **3**) from migrating to TCTA, which has a lower triplet energy. *p*-Bis(triphenylsilyl)benzene (UGH2)[8] doped with 10 wt% of iridium complex, 2,9-dimethyl-4,7-diphenyl-1,10-phenanthroline (BCP)[15] or 3-(biphenyl-4-yl)-4-phenyl-5-(4-*tert*-butylphenyl)-1,2,4-triazole (TAZ),[8] and LiF were used as the emitting, electron-transport, and electron-injection layers, respectively.

The current-voltage-brightness (I-V-L) characteristics and external quantum efficiencies of devices A1 and A2 are shown in Table 4 and in Figure 8a,b. The relatively lower operation voltage of device A2 compared with A1 is probably attributed to the reduction in the thicknesses of the large-gap CzSi and UGH2 layers. Device A1 shows a maximum external EL quantum efficiency of 2.3% photon/electron (2.9 cdA^{-1}, maximum) and a maximal power efficiency of 1.5 lmW^{-1}. Device A2 shows a maximum external EL quantum efficiency of 1.3% photon/electron (2.5 cdA^{-1}, maximum) and a maximal power efficiency of 1.9 lmW^{-1}. Both

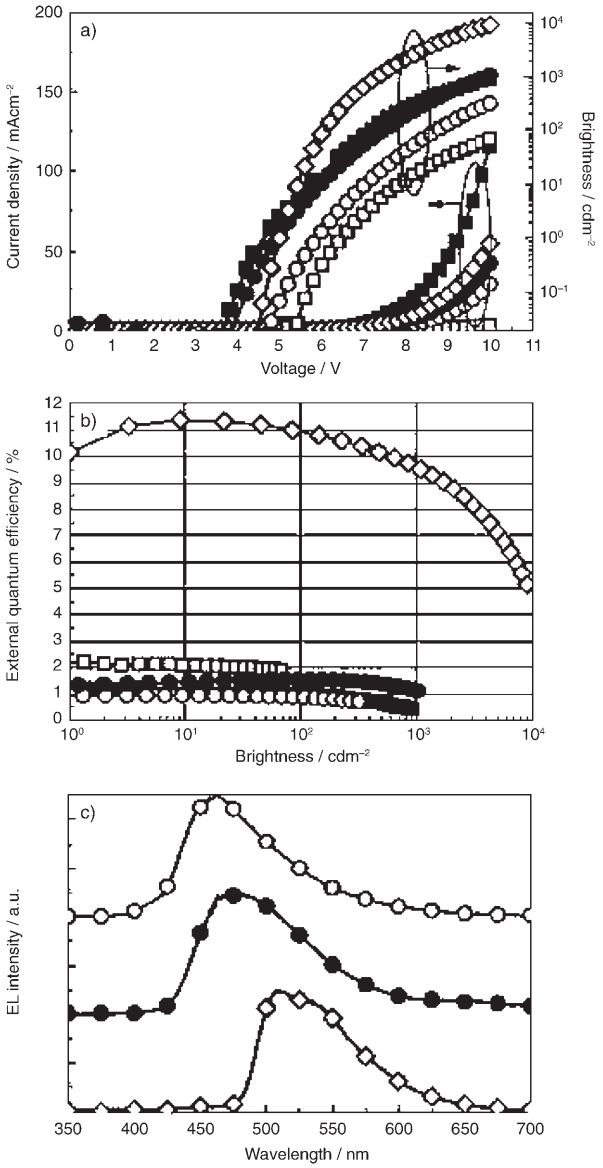

Figure 8. a) I-V-L characteristics, b) device efficiencies compared with the brightness of the devices, and c) EL spectra of devices B1, B2, and C. □ = device A1; ■ = device A2; ○ = device B1; ● = device B2; ◇ = device C.

the EL spectra of devices A1 and A2 showed strong emissions from adjacent transporting layers, which indicates a less-balanced carrier injection. Such a factor, along with the lower quantum yields of the complexes, might be the reason for the lower device efficiencies.

The nondoped device architectures were also fabricated for complexes **1** and **3**.[16] The layer structures consist of ITO/PEDOT (≈300 Å)/αNPD (150 Å)/TCTA (150 Å)/complex **1** or **3** (200 Å)/BCP (500 Å)/LiF (5 Å)/Al (1200 Å) for devices B1 and B2, in which the conducting polymer polyethylene dioxythiophene/polystyrene sulfonate (PEDOT) was utilized as the hole-injection layer.[17]

The EL spectra, I-V-L characteristics and external quantum efficiencies of devices B1 and B2 are also shown in Figure 8. As can be seen from Figure 8c, the EL spectra of the devices are similar to the photoluminescence (PL) spectra of the complexes in CH_2Cl_2 solution. In contrast with the devices A1 and A2, this indicates that the devices B1 and B2 are more effective in injecting both holes and electrons into the emitting layer and that the iridium complexes have adequate carrier-transporting properties. The applied operation voltages at 10 $mAcm^{-2}$ for the devices B1 and B2 are 9.0 and 8.5 V, respectively. Such an observation is consistent with the electrochemical results in which complex **3** shows a slightly lowered oxidation potential, and the relatively smaller energy barrier for hole injection into the emitting layer for **3** contributes in reducing the operation voltage. A maximum external quantum conversion efficiency (EQE) of 1.0% photon/electron, luminous efficiency of 1.5 cdA^{-1}, and power efficiency of 0.9 lmW^{-1} were obtained for device B1 at 10 cdm^{-2}, whereas the maximum efficiencies of 1.6% photon/electron, 3.4 cdA^{-1}, and 1.9 lmW^{-1} were obtained for device B2 at 150 cdm^{-2}, respectively.

Encouraged by the results of devices B1 and B2, we have conducted an experiment using the above-mentioned iridium complex as the host material for the fabrication of green phosphorescent OLEDs. This is attributed to its high triplet excited-state energy, which could allow the effective excitation and confinement of triplet excited states on the dopant molecules. The associated device architecture consists of ITO/PEDOT (≈30 nm)/αNPD (30 nm)/TCTA (5 nm)/**1** doped with 2 wt% $[Ir(ppy)_3]$ (20 nm; ppyH = 2-phenylpyridine)/TAZ (50 nm)/LiF (0.5 nm)/Al (120 nm), which is similar to the previously mentioned nondoped devices, except that a blend of **1** and 2 wt% of $[Ir(ppy)_3]$ was used as the emitting layer and that TAZ was selected as the electron-transport layer.[18]

As shown in Figure 8c, the EL spectrum of device C is now dominated by emission from $[Ir(ppy)_3]$, which indicates the effectiveness of the present device structure in injecting both holes and electrons into the emitting layer. The I-V-L characteristics and external EL quantum efficiency are also shown in Figure 8a,b. The turn-on voltage of device C is 5 V (defined as the voltage at 1 cdm^{-2}). The device has an external quantum efficiency of up to 11.4% photons per electron (36.6 cdA^{-1}, maximum), a peak power efficiency of 21.7 lmW^{-1}, and a maximum brightness of 32000 cdm^{-2} at 14.5 V. It should be noted that reports of phosphorescent OLEDs with phosphorescent organometallic complexes as host materials are very rare. Among the few previous reports, red phosphorescent OLEDs reported by Tsuzuki and Tokito,[19] for which $[Ir(acac)(ppy)_2]$ and $[Ir(piq)_3]$ (acac = acetylacetonate, piqH = 1-phenylisoquinoline) were utilized as the host and the guest, gave the highest external quantum efficiency of 9.2%. However, the study herein indicates, for the first time, that a phosphorescent organometallic complex can be used as the host material for much higher-energy, green phosphorescent electroluminescence. Furthermore, the major energy-transfer mechanism from a phosphorescent organometallic complex host to a triplet emitter is the Förster energy transfer, rather than the Dexter energy transfer from a conventional fluorescent host to a triplet emitter, which usually requires a rather high dopant concentration (e.g. 8–10 wt%) to ensure effective energy transfer.[20] Thus, in using the phosphorescent organometallic complexes as hosts, the emitting dopant concentration can be substantially reduced (e.g. 2 wt% in the present case). Consequently, efficiency roll-off at higher brightness, which is typical in phosphorescent OLEDs and may be associated with triplet–triplet annihilation, may be alleviated. For instance, in the present device, the device quantum efficiency remains rather constant over a wide brightness range of 1–1000 cdm^{-2}.

Conclusion

We report the preparation, basic photophysical properties, and potential OLED applications of the iridium(III) complexes **1**–**4** that bear one blue-emitting chromophore and two nonconjugated cyclometalated N-benzylpyrazoles that possess a much greater ligand energy gap. It is notable that the resulting metal complexes show unexpected isomerization in solution, which is caused by the restricted twist motion involving the methylene units. Despite this fluxional motion in solution, their photophysical data support the concept of introducing the methylene spacer into the cyclometalated ligand to break the π conjugation of chelating ligands, the result of which then lowers the π orbital energies and destabilizes the respective π* orbitals of the nonconjugated chelates. By using complex **1** as a prototype, doped phosphorescent OLED devices that use these complexes as emitters have been successfully made, exhibiting a blue EL with 1931 Commission Internationale de L'Eclairage (CIE) coordinates of (0.19, 0.21), albeit with much lower device efficiencies. On the other hand, it is impressively explored that these blue-emitting complexes could be used as the host material for green phosphorescent OLEDs. The efficiency and photon/electron rate of the as-fabricated device reach 11% and 18 lmW^{-1}, respectively, at the practical brightness of 100 cdm^{-2}. Thus, with the assistance of this nonconjugation designing principle and the incorporation of the third chelating chromophores with an appropriate energy gap, the desired blue-emitting materials as well as phosphorescent OLEDs that employ these materials as

hosts for lower-energy phosphorescent dopants can be successfully prepared.

Experimental Section

General information and materials: Mass spectra were obtained on a JEOL SX-102A instrument operating in fast atom bombardment (FAB) mode. ^{1}H and ^{19}F NMR spectra were recorded on Varian Mercury-400 or INOVA-500 instruments; chemical shifts are quoted with respect to the internal standard tetramethylsilane for ^{1}H data. Elemental analyses were carried out at the NSC Regional Instrumentation Center at the National Chao Tung University, Hsinchu (Taiwan). The 2-pyridyl azolate chelates, namely: 3-trifluoromethyl-5-(2-pyridyl)-1,2,4-triazole (fptz)H, 3-phenyl-5-(4-*t*-butyl-2-pyridyl)-1,2,4-triazole (pbptz)H, and 3-*t*-butyl-5-(4-*t*-butyl-2-pyridyl)-1,2,4-triazole (bbptz)H were prepared by using methods that are documented in the literature.[21] All reactions were conducted under a N_2 atmosphere by using anhydrous solvents or solvents treated with an appropriate drying reagent.

Preparation of (dfb-pz)H: Pyrazole (3.42 g, 50.2 mmol) was added to a suspension of NaH (1.31 g, 54.8 mmol) in THF (25 mL) at 0 °C and under N_2. The mixture was stirred until the evolution of hydrogen had ceased. A solution of 2,4-difluorobenzyl bromide (6.0 mL, 45.7 mmol) in dry THF (10 mL) was added dropwise. The reaction mixture was stirred at room temperature for 12 h, from which the white precipitate was removed by filtration. The pure product was then obtained after column chromatography by using ethyl acetate as the eluent to give 7.26 g of a light-yellow liquid (38.8 mmol, 84 %). The second ligand, (tfmfb-pz)H, was prepared in 90 % yield by employing 2-trifluoromethyl-5-fluorobenzyl bromide as the alternative starting material.

Ligand (dfb-pz)H: ^{1}H NMR (400 MHz, $CDCl_3$, 294 K): δ = 7.52 (d, J = 2.0 Hz, 1H; CH), 7.42 (d, J = 2.0 Hz, 1H; CH), 7.15–7.10 (m, 1H; CH), 6.85–6.79 (m, 2H; CH), 6.26 (t, J = 2.0 Hz, 1H; CH), 5.30 ppm (s, 2H; CH_2).

Ligand (tfmfb-pz)H: ^{1}H NMR (300 MHz, $CDCl_3$, 294 K): δ = 7.67 (m, 2H; CH), 7.44 (d, J = 2.0 Hz, 1H; CH), 7.03 (t, J = 7.8 Hz, 1H; CH), 6.50 (d, J = 9.5 Hz, 1H; CH), 6.35 (t, J = 2.0 Hz, 1H; CH), 5.53 ppm (s, 2H; CH_2).

Preparation of [Ir(dfb-pz)$_2$(fptz)] (1): A mixture of (dfb-pz)H (0.35 g, 1.79 mmol) and $IrCl_3 \cdot 3H_2O$ (0.30 g, 0.851 mmol) in 2-methoxyethanol (5 mL) was refluxed for 24 h under nitrogen. After cooling the solution to room temperature, 3-trifluoromethyl-5-(2-pyridyl) triazole (182 mg, 0.851 mmol) and Na_2CO_3 (90 mg, 0.851 mmol) were added and the mixture was stirred at room temperature for a further 12 h. An excess of water was added and the resulting precipitate was collected by filtration and washed with MeOH and ether. Further purification was conducted by recrystallization with acetone/hexane to give 0.40 g of white crystals (0.501 mmol, 59 %). ^{1}H NMR (500 MHz, [D$_6$]acetone, 193 K): δ = 8.92 (d, J = 5.5 Hz, 1H; CH), 8.31 (d, J = 2.0 Hz, 1H; CH), 8.25 (d, J = 2.0 Hz, 1H; CH), 8.22 (t, J = 7.5 Hz, 1H; CH), 8.15 (d, J = 7.5 Hz, 1H; CH), 7.71 (t, J = 6.0 Hz, 1H; CH), 7.38 (d, J = 1.5 Hz, 1H; CH), 6.97 (d, J = 1.5 Hz, 1H; CH), 6.73 (td, J = 9.5 Hz, 2.0 Hz, 1H; CH), 6.61 (td, J = 9.5 Hz, 2.0 Hz, 1H; CH), 6.43 (t, J = 2.0 Hz, 1H; CH), 6.36 (t, J = 2.0 Hz, 1H; CH), 5.99 (d, J = 16.0 Hz, 1H; CH_2), 5.91 (d, J = 14.5 Hz, 1H; CH_2), 5.74 (d, J = 14.5 Hz, 1H; CH_2), 5.08–5.04 (m, 2H; CH,CH_2), 4.73 ppm (dd, J = 9.5 Hz, 2.0 Hz, 1H; CH); ^{19}F NMR (470 MHz, [D$_6$]acetone, 294 K): δ = −63.85 (s, 3F; CF_3), −115.03 (s, 1F; CF), −115.99 (s, 1F; CF), −118.15 (s, 1F; CF), −120.11 ppm (s, 1F; CF); MS (FAB): m/z: 793 $[M+1]^+$; elemental analysis calcd (%) for $C_{28}H_{18}F_7IrN_8$: N 14.15, C 42.48, H 2.29; found: N 13.93, C 42.28, H 2.62.

Preparation of [Ir(dfb-pz)$_2$(pbptz)] (2): Compound **2** was obtained in 40 % yield by a similar procedure to that described for the parent compound **1**. Purification was conducted by silica-gel column chromatography by using CH_2Cl_2 as the eluent. ^{1}H NMR (400 MHz, [D$_6$]acetone, 294 K): δ = 8.62 (d, J = 5.4 Hz, 1H; CH), 8.18–8.15 (m, 3H; CH), 8.13 (d, J = 2.4 Hz, 1H; CH), 8.08 (d, J = 2.4 Hz, 1H; CH), 7.58 (dd, J = 6.0 Hz, 2.4 Hz, 1H; CH), 7.40–7.27 (m, 2H; CH), 7.29 (td, J = 7.6 Hz, 2.0 Hz, 1H; CH), 7.19–7.16 (m, 2H; CH), 6.55 (ddd, J = 10.4 Hz, 9.2 Hz, 2.4 Hz, 1H; CH), 6.44 (ddd, J = 10.4 Hz, 9.2 Hz, 2.4 Hz, 1H; CH), 6.30 (t, J = 2.4 Hz, 1H; CH), 6.25 (t, J = 2.4 Hz, 1H; CH), 6.12–5.61 (br s, 2H; CH,CH_2), 5.38–5.07 (br s, 4H; CH), 1.40 ppm (s, 9H; CH_3); MS (FAB): m/z: 857 $[M+1]^+$; elemental analysis calcd (%) for $C_{37}H_{31}F_4IrN_8 \cdot CH_2Cl_2$: N 11.91, C 48.51, H 3.54; found: N 12.08, C 48.60, H 3.75.

Preparation of [Ir(bbptz)(dfb-pz)$_2$] (3): Compound **3** was obtained in 63 % yield by a procedure similar to that described for the parent compound **1**. Purification was conducted by flash column chromatography with CH_2Cl_2 as the eluent. ^{1}H NMR (400 MHz, [D$_6$]acetone, 294 K): δ = 8.60 (d, J = 6.0 Hz,1H; CH), 8.11 (d, J = 2.4 Hz, 1H; CH), 8.06 (d, J = 2.4 Hz, 1H; CH), 7.99 (s, 1H; CH), 7.52 (dd, J = 6.0 Hz, 2.4 Hz, 1H; CH), 7.18 (s, 1H; CH), 7.12 (br s, 1H; CH), 6.52 (ddd, J = 10.8 Hz, 8.8 Hz, 2.4 Hz, 1H; CH), 6.39 (ddd, J = 10.4 Hz, 9.2 Hz, 2.4 Hz, 1H; CH), 6.30 (t, J = 2.4 Hz, 1H; CH), 6.25 (t, J = 2.4 Hz, 1H; CH), 6.12 (d, J = 15.6 Hz, 1H; CH_2), 5.84–5.26 (br s, 3H; CH,CH_2), 5.01–4.88 (m, 2H; CH,CH_2), 1.37 (s, 9H; CH_3), 1.35 ppm (s, 9H; CH_3); MS (FAB): m/z: 837 $[M+1]^+$; elemental analysis calcd (%) for $C_{35}H_{35}F_4IrN_8 \cdot 0.5\,CH_2Cl_2$: N 12.76, C 48.54, H 4.13; found: N 12.55, C 48.16, H 4.25.

Preparation of [Ir(fptz)(tfmfb-pz)$_2$] (4): A mixture of (tfmfb-pz)H (208 mg, 0.85 mmol) and $[IrCl_3] \cdot 3H_2O$ (150 mg, 0.43 mmol) in 2-methoxyethanol (4 mL) was refluxed for 2 d under nitrogen. After cooling the solution to room temperature, 3-trifluoromethyl-5-(2-pyridyl) triazole (91 mg, 0.43 mmol) and Na_2CO_3 (45 mg, 0.43 mmol) were added and the mixture was stirred at room temperature for a further 12 h. After this time, an excess of water was added and the resulting precipitate was collected by filtration. Further purification was conducted by column chromatography with an eluent consisting of a 1:3 mixture of CH_2Cl_2 and hexane. The resulting white powder was recrystallized from CH_2Cl_2/hexane at room temperature to give 120 mg of a white crystalline product (0.13 mmol, 32 %). ^{1}H NMR (400 MHz, [D$_6$]acetone, 294 K): δ = 8.96 (d, J = 5.2 Hz, 1H$_{4a}$; CH), 8.50 (d, J = 8.0 Hz, 1H$_{4b}$; CH), 8.28 (t, J = 7.6 Hz, 1H$_{4b}$; CH), 8.22–8.14 (m, 1H$_{4a}$ + 2H$_{4b}$; CH), 8.07 (m, 1H$_{4b}$; CH), 8.02–7.97 (m, 2H$_{4a}$ + 2H$_{4b}$; CH), 7.73 (m, 1H$_{4a}$; CH), 7.52–7.28 (m, 2H$_{4a}$ + 5H$_{4b}$; CH), 7.13 (d, J = 2.4 Hz, 1H$_{4a}$; CH), 6.91 (t, J = 8.4 Hz, 1H$_{4b}$; CH), 6.75 (t, J = 8.4 Hz, 1H$_{4b}$; CH), 6.70 (dd, J = 8.4 Hz, 2.4 Hz, 1H$_{4a}$; CH), 6.47 (t, J = 8.8 Hz, 1H$_{4a}$; CH), 6.37–6.31 (m, 2H$_{4a}$; CH,CH_2), 6.25–6.21 (m, 3H$_{4a}$; CH), 5.77 (d, J = 16.4 Hz, 1H$_{4a}$; CH_2), 5.72 (d, J = 16.4 Hz, 1H$_{4a}$; CH_2), 5.42 (d, J = 15.2 Hz, 1H$_{4b}$; CH_2), 5.36 (d, J = 15.2 Hz, 1H$_{4b}$; CH_2), 5.31 (d, J = 16.4 Hz, 1H$_{4a}$; CH_2), 4.88 (d, J = 15.2 Hz, 1H$_{4b}$; CH_2), 4.79 ppm (d, J = 15.2 Hz, 1H$_{4b}$; CH_2); ^{19}F NMR (470 MHz, [D$_6$]acetone, 294 K): δ = −57.21 (s, 6F$_{4a}$; CF_3), −57.54 (s, 3F$_{4b}$; CF_3), −57.67 (s, 3F$_{4b}$; CF_3), −63.70 (s, 3F$_{4b}$; CF_3), −64.03 (s, 3F$_{4a}$; CF_3), −88.72 (s, 1F$_{4b}$; CF), −91.34 (s, 1F$_{4a}$; CF), −91.85 (s, 1F$_{4b}$; CF), −94.87 (s, 1F$_{4a}$; CF); MS (FAB): m/z: 893 $[M+1]^+$; elemental analysis calcd (%) for $C_{30}H_{18}F_{11}IrN_8 \cdot CH_2Cl_2$: N 11.47, C 38.12, H 2.06; found: N 11.45, C 38.31, H 2.37.

X-ray crystal structural determination: Single-crystal X-ray diffraction data were measured on a Bruker SMART CCD diffractometer ($2\theta_{max} \leq$ 55.0°, ω scan mode) equipped with a graphite monochromator. The data collection was executed by using the SMART program. Cell refinement and data reduction were accomplished by using the SAINT program. The structures were solved by using the SHELXTL/PC package and refined by using full-matrix least-squares. An empirical absorption correction was applied with the SADABS routine (part of the SHELXTL program). The structure was solved by direct methods by using the SHELXTL suite of programs. All non-hydrogen atoms were refined anisotropically by full-matrix least-squares on F^2. Hydrogen atoms were placed in calculated positions and allowed to ride on the parent atoms.

Selected crystal data for ***1***: $C_{28}H_{18}F_7IrN_8$; M = 791.70; orthorhombic; space group = $P2_12_12_1$; a = 10.3093(5), b = 13.6403(7), c = 18.7989(9) Å; V = 2643.54(20) Å^3; Z = 4; ρ_{calcd} = 1.989 g cm^{-1}; $F(000)$ = 1528; crystal size = 0.13 × 0.10 × 0.10 mm^3; $\lambda(Mo_{K\alpha})$ = 0.71073 Å; T = 150(2) K; μ = 5.137 mm^{-1}; index ranges $-13 \leq h \leq 13$, $-17 \leq k \leq 17$, $-21 \leq l \leq 24$, 20456 reflections collected, 6067 with R(int) = 0.0546, final wR_2(all data) = 0.0578, $R_1[I > 2\sigma(I)]$ = 0.0302.

Selected crystal data for ***4***: $C_{31}H_{20}Cl_2F_{11}IrN_8$; M = 976.65; triclinic; space group = $P\bar{1}$; a = 11.0573(6), b = 12.3430(6), c = 13.4708(7) Å; α =

101.603(1), $\beta = 112.153(1)$, $\gamma = 94.582(1)°$; $V = 1643.23(15)$ Å^3; $Z = 2$; $\rho_{calcd} = 1.974$ gcm^{-1}; $F(000) = 944$; crystal size $= 0.25 \times 0.15 \times 0.15$ mm^3; $\lambda(Mo_{K\alpha}) = 0.71073$ Å; $T = 150(2)$ K; $\mu = 4.327$ mm^{-1}; index ranges $-14 \le h \le 14$, $-16 \le k \le 16$, $-17 \le l \le 17$; 21693 reflections collected, 7532 with $R(\text{int}) = 0.0339$, final $wR_2(\text{all data}) = 0.0573$, $R_1[I > 2\sigma(I)] = 0.0253$.

CCDC-677848 (**1**) and -677849 (**4**) contain the supplementary crystallographic data for this paper. These data can be obtained free of charge from The Cambridge Crystallographic Data Centre via www.ccdc.cam.ac.uk/data_request/cif

Spectral measurements: Steady-state absorption and emission spectra were recorded by a Hitachi (U-3310) spectrophotometer and an Edinburgh (FS920) fluorimeter, respectively. Solution samples were degassed by three freeze–pump–thaw cycles. Quinine sulfate with an emission yield of $\Phi \approx 0.57$ ($\lambda_{max} \approx 460$ nm) in 0.1 M H_2SO_4 was used as a reference to determine quantum yields for the studied compounds in solution. Equation (1) was used to calculate the emission quantum yields.

$$\Phi_s = \Phi_r \left(\frac{\eta_s^2 A_r I_s}{\eta_r^2 A_s I_r} \right) \quad (1)$$

In Equation (1), Φ_s and Φ_r are the quantum yields of the unknown and reference samples, η is the refractive index of the solvent, A_r and A_s are the absorbance of the reference and the unknown samples at the excitation wavelength, and I_s and I_r are the integrated areas under the emission spectra of interest, respectively.

Lifetime studies were performed with an Edinburgh FL 900 photon counting system by using a hydrogen-filled or a nitrogen lamp as the excitation source. Data were analyzed by using the nonlinear least-squares procedure in combination with an iterative convolution method. The emission decays were analyzed by the sum of exponential functions, which allows partial removal of the instrument time-broadening and consequently renders a temporal resolution of about 200 ps.

Computational methodology: All the calculations were carried out by using a Gaussian 03 (G03) program package.[22] Calculations on the electronic ground state of complexes **1**–**4** were carried out by using the DFT method with B3LYP density functional theory.[23,24] The Hay–Wadt double-ζ with a Los Alamos relativistic effect core potential basis set LANL2DZ[25] was employed for the Ir atom, and the other atoms were described by a split valence Pople basis (6-31G).[26] The relativistic effective core potential (ECP) replaced the inner core electrons of Ir(III), leaving the outer core ($5s^25p^6$) electrons and the $5d^6$ valence electrons. The basis set was described as Ir (8s6p3d)/[3s3p2d], C, N, and F (10s,4p,1d)/[3s,2p,1d], and H (4s)/[2s].[2s] On the basis of the optimized geometry in the ground state, the absorption and emission properties in CH_2Cl_2 can be calculated by TD-DFT[27] with the polarized continuum model (PCM), as implemented in G03. Within TD-DFT, the description of the excited states is based on a linear combination of singly occupied-to-virtual orbital excitations and thereby provides information beyond a simple HOMO–LUMO picture. Compositions of molecular orbitals, overlap populations between molecular fragments, bond orders, and density-of-states spectra were calculated by using the AOMix program.[28]

Device fabrication and characterization: OLEDs were fabricated on ITO-coated glass substrates with multiple organic layers sandwiched between the transparent bottom ITO anode and the top metal cathode. The PEDOT layer was prepared by spin coating, whereas other layers were fabricated by vacuum evaporation in a vacuum chamber with a base pressure of less than 10^{-6} torr. The deposition system permits the fabrication of the complete multilayer device structure in a single vacuum pump-down without breaking the vacuum. The deposition rate of organic layers was kept at approximately 0.2 nms^{-1}. The active area of the device is 1×1 mm^2, as defined by the shadow mask for cathode deposition. The I-V-L characteristics of devices were measured by using an Agilent 4155B semiconductor parameter analyzer and a Si photodiode calibrated with Photo Research PR-650 spectroradiometer. EL spectra of devices were collected by a calibrated CCD spectrograph.

Acknowledgements

We thank the National Science Council for financial support (research grants: NSC 91–2119M-002—016 and 94-EC-17 A-08-S1—042) and the National Center for High-Performance Computing for computer time and facilities.

[1] a) H. Yersin, *Top. Curr. Chem.* **2004**, *241*, 1–26; b) E. Holder, B. M. W. Langeveld, U. S. Schubert, *Adv. Mater.* **2005**, *17*, 1109–1121; c) P.-T. Chou, Y. Chi, *Eur. J. Inorg. Chem.* **2006**, 3319–3332; d) Y. Sun, N. C. Giebink, H. Kanno, B. Ma, M. E. Thompson, S. R. Forrest, *Nature* **2006**, *440*, 908–912; e) R. C. Evans, P. Douglas, C. J. Winscom, *Coord. Chem. Rev.* **2006**, *250*, 2093–2126; f) L. Flamigni, A. Barbieri, C. Sabatini, B. Ventura, F. Barigelletti, *Top. Curr. Chem.* **2007**, *281*, 143–203.

[2] a) M. A. Baldo, D. F. O'Brien, Y. You, A. Shoustikov, S. Sibley, M. E. Thompson, S. R. Forrest, *Nature* **1998**, *395*, 151–154; b) S. Lamansky, P. Djurovich, D. Murphy, F. Abdel-Razzaq, H.-E. Lee, C. Adachi, P. E. Burrows, S. R. Forrest, M. E. Thompson, *J. Am. Chem. Soc.* **2001**, *123*, 4304–4312.

[3] a) P. Coppo, E. A. Plummer, L. De Cola, *Chem. Commun.* **2004**, 1774–1775; b) M. K. Nazeeruddin, R. Humphry-Baker, D. Berner, S. Rivier, L. Zuppiroli, M. Graetzel, *J. Am. Chem. Soc.* **2003**, *125*, 8790–8797; c) Y. You, S. Y. Park, *J. Am. Chem. Soc.* **2005**, *127*, 12438–12439; d) R. Ragni, E. A. Plummer, K. Brunner, J. W. Hofstraat, F. Babudri, G. M. Farinola, F. Naso, L. De Cola, *J. Mater. Chem.* **2006**, *16*, 1161–1170; e) S.-C. Lo, C. P. Shipley, R. N. Bera, R. E. Harding, A. R. Cowley, P. L. Burn, I. D. W. Samuel, *Chem. Mater.* **2006**, *18*, 5119–5129; f) M. K. Nazeeruddin, M. Gratzel, *Struct. Bonding (Berlin)* **2007**, *123*, 113–175; g) K. Dedeian, J. Shi, E. Forsythe, D. C. Morton, P. Y. Zavalij, *Inorg. Chem.* **2007**, *46*, 1603–1611.

[4] a) R. J. Holmes, S. R. Forrest, Y.-J. Tung, R. C. Kwong, J. J. Brown, S. Garon, M. E. Thompson, *Appl. Phys. Lett.* **2003**, *82*, 2422–2424; b) S. Tokito, T. Iijima, Y. Suzuri, H. Kita, T. Tsuzuki, F. Sato, *Appl. Phys. Lett.* **2003**, *83*, 569–571.

[5] Y. You, S. H. Kim, H. K. Jung, S. Y. Park, *Macromolecules* **2006**, *39*, 349–356.

[6] X. Ren, J. Li, R. J. Holmes, P. I. Djurovich, S. R. Forrest, M. E. Thompson, *Chem. Mater.* **2004**, *16*, 4743–4747.

[7] a) S.-J. Yeh, W.-C. Wu, C.-T. Chen, Y.-H. Song, Y. Chi, M.-H. Ho, S.-F. Hsu, C.-H. Chen, *Adv. Mater.* **2005**, *17*, 285–289; b) P.-T. Chou, Y. Chi, *Chem. Eur. J.* **2007**, *13*, 380–395.

[8] C.-H. Yang, Y.-M. Cheng, Y. Chi, C.-J. Hsu, F.-C. Fang, K.-T. Wong, P.-T. Chou, C.-H. Chang, M.-H. Tsai, C.-C. Wu, *Angew. Chem.* **2007**, *119*, 2470–2473; *Angew. Chem. Int. Ed.* **2007**,*46*, 2418–2421.

[9] a) W.-Y. Wong, C.-L. Ho, Z.-Q. Gao, B.-X. Mi, C.-H. Chen, K.-W. Cheah, Z. Lin, *Angew. Chem.* **2006**, *118*, 7964–7967; *Angew. Chem. Int. Ed.* **2006**, *45*, 7800–7803; b) T.-H. Kwon, H. S. Cho, M. K. Kim, J.-W. Kim, J.-J. Kim, K. H. Lee, S. J. Park, I.-S. Shin, H. Kim, D. M. Shin, Y. K. Chung, J.-I. Hong, *Organometallics* **2005**, *24*, 1578–1585; c) W.-Y. Wong, G.-J. Zhou, X.-M. Yu, H.-S. Kwok, B.-Z. Tang, *Adv. Funct. Mater.* **2006**, *16*, 838–846; d) W.-Y. Wong, G.-J. Zhou, X.-M. Yu, H.-S. Kwok, Z. Lin, *Adv. Funct. Mater.* **2007**, *17*, 315–323; e) C.-L. Ho, W.-Y. Wong, G.-J. Zhou, B. Yao, Z. Xie, L. Wang, *Adv. Funct. Mater.* **2007**, *17*, 2925–2936.

[10] S. Lamansky, P. Djurovich, D. Murphy, F. Abdel-Razzaq, R. Kwong, I. Tsyba, M. Bortz, B. Mui, R. Bau, M. E. Thompson, *Inorg. Chem.* **2001**, *40*, 1704–1711.

[11] a) A. Tsuboyama, H. Iwawaki, M. Furugori, T. Mukaide, J. Kamatani, S. Igawa, T. Moriyama, S. Miura, T. Takiguchi, S. Okada, M. Hoshino, K. Ueno, *J. Am. Chem. Soc.* **2003**, *125*, 12971–12979; b) T. Sajoto, P. I. Djurovich, A. Tamayo, M. Yousufuddin, R. Bau, M. E. Thompson, R. J. Holmes, S. R. Forrest, *Inorg. Chem.* **2005**, *44*, 7992–8003; c) F.-M. Hwang, H.-Y. Chen, P.-S. Chen, C.-S. Liu, Y. Chi, C.-F. Shu, F.-I. Wu, P.-T. Chou, S.-M. Peng, G.-H. Lee, *Inorg. Chem.* **2005**, *44*, 1344–1353.

[12] a) E. Orselli, G. S. Kottas, A. E. Konradsson, P. Coppo, R. Froehlich, L. De Cola, A. van Dijken, M. Buechel, H. Boerner, *Inorg. Chem.* **2007**, *46*, 11082–11093; b) I. Avilov, P. Minoofar, J. Cornil, L. De Cola, *J. Am. Chem. Soc.* **2007**, *129*, 8247–8258.
[13] F. De Angelis, S. Fantacci, N. Evans, C. Klein, S. M. Zakeeruddin, J.-E. Moser, K. Kalyanasundaram, H. J. Bolink, M. Graetzel, M. K. Nazeeruddin, *Inorg. Chem.* **2007**, *46*, 5989–6001.
[14] a) C.-H. Yang, S.-W. Li, Y. Chi, Y.-M. Cheng, Y.-S. Yeh, P.-T. Chou, G.-H. Lee, C.-H. Wang, C.-F. Shu, *Inorg. Chem.* **2005**, *44*, 7770–7780; b) Y. You, K. S. Kim, T. K. Ahn, D. Kim, S. Y. Park, *J. Phys. Chem. C* **2007**, *111*, 4052–4060; c) C.-J. Chang, C.-H. Yang, K. Chen, Y. Chi, C.-F. Shu, M.-L. Ho, Y.-S. Yeh, C. Pi-Tai, *Dalton Trans.* **2007**, 1881–1890.
[15] D. F. O'Brien, M. A. Baldo, M. E. Thompson, S. R. Forrest, *Appl. Phys. Lett.* **1999**, *74*, 442–444.
[16] R. J. Holmes, B. W. D'Andrade, S. R. Forrest, X. Ren, J. Li, M. E. Thompson, *Appl. Phys. Lett.* **2003**, *83*, 3818–3820.
[17] A. Elscher, F. Bruder, H.-W. Heuer, F. Jonas, A. Karbach, S. Kirchmeyer, S. Thurm, R. Wehrmann, *Synth. Met.* **2000**, *111*, 139–143.
[18] J. Kido, M. Kimura, K. Nagai, *Science* **1995**, *267*, 1332–1334.
[19] T. Tsuzuki, S. Tokito, *Adv. Mater.* **2007**, *19*, 276–280.
[20] a) R. C. Kwong, S. Lamansky, M. E. Thompson, *Adv. Mater.* **2000**, *12*, 1134–1138; b) T. Tsuzuki, Y. Nakayama, J. Nakamura, T. Iwata, S. Tokito, *Appl. Phys. Lett.* **2006**, *88*, 243511–243513.
[21] a) S. Kubota, M. Uda, T. Nakagawa, *J. Heterocycl. Chem.* **1975**, *12*, 855–860; b) K. Funabiki, N. Noma, G. Kuzuya, M. Matsui, K. Shibata, *J. Chem. Res. (M)*, **1999**, 1301–1308.
[22] Gaussian 03, Revision C.02, M. J. Frisch, G. W. Trucks, H. B. Schlegel, G. E. Scuseria, M. A. Robb, J. R. Cheeseman, J. A. Montgomery, Jr., T. Vreven, K. N. Kudin, J. C. Burant, J. M. Millam, S. S. Iyengar, J. Tomasi, V. Barone, B. Mennucci, M. Cossi, G. Scalmani, N. Rega, G. A. Petersson, H. Nakatsuji, M. Hada, M. Ehara, K. Toyota, R. Fukuda, J. Hasegawa, M. Ishida, T. Nakajima, Y. Honda, O. Kitao, H. Nakai, M. Klene, X. Li, J. E. Knox, H. P. Hratchian, J. B. Cross, V. Bakken, C. Adamo, J. Jaramillo, R. Gomperts, R. E. Stratmann, O. Yazyev, A. J. Austin, R. Cammi, C. Pomelli, J. W. Ochterski, P. Y. Ayala, K. Morokuma, G. A. Voth, P. Salvador, J. J. Dannenberg, V. G. Zakrzewski, S. Dapprich, A. D. Daniels, M. C. Strain, O. Farkas, D. K. Malick, A. D. Rabuck, K. Raghavachari, J. B. Foresman, J. V. Ortiz, Q. Cui, A. G. Baboul, S. Clifford, J. Cioslowski, B. B. Stefanov, G. Liu, A. Liashenko, P. Piskorz, I. Komaromi, R. L. Martin, D. J. Fox, T. Keith, M. A. Al-Laham, C. Y. Peng, A. Nanayakkara, M. Challacombe, P. M. W. Gill, B. Johnson, W. Chen, M. W. Wong, C. Gonzalez, J. A. Pople, Gaussian, Inc., Wallingford CT, **2004**.
[23] C. Lee, W. Yang, R. G. Parr, *Phys. Rev. B* **1988**, *37*, 785–789.
[24] A. D. Becke, *J. Chem. Phys.* **1993**, *98*, 5648–5652.
[25] a) P. J. Hay, W. R. Wadt, *J. Chem. Phys.* **1985**, *82*, 270–283; b) W. R. Wadt, P. J. Hay, *J. Chem. Phys.* **1985**, *82*, 284–298; c) P. J. Hay, W. R. Wadt, *J. Chem. Phys.* **1985**, *82*, 299–310.
[26] P. C. Hariharan, J. A. Pople, *Mol. Phys.* **1974**, *27*, 209–214.
[27] a) C. Jamorski, M. E. Casida, D. R. Salahub, *J. Chem. Phys.* **1996**, *104*, 5134–5147; b) M. Petersilka, U. J. Grossmann, E. K. U. Gross, *Phys. Rev. Lett.* **1996**, *76*, 1212–1215; c) R. Bauernschmitt, R. Ahlrichs, F. H. Hennrich, M. M. Kappes, *J. Am. Chem. Soc.* **1998**, *120*, 5052–5059; d) M. E. Casida, *J. Chem. Phys.* **1998**, *108*, 4439–4449; e) R. E. Stratmann, G. E. Scuseria, M. J. Frisch, *J. Chem. Phys.* **1998**, *109*, 8218–8224.
[28] a) S. I. Gorelsky, *AOMix*: Program for Molecular Orbital Analysis, http://www.sg-chem.net, University of Ottawa (US), **2007**; b) S. I. Gorelsky, A. B. P. Lever, *J. Organomet. Chem.* **2001**, *635*, 187–196.
[29] V. A. Polyakov, A. D. Ryabov, *J. Chem. Soc. Dalton Trans.* **1986**, *12*, 589.

Received: January 10, 2008
Published online: April 18, 2008

